# DIRECT NUMERICAL SIMULATION OF TURBULENT CONVECTION IN A RECTANGULAR RAYLEIGH-BÉNARD CELL

**Matthias Kaczorowski**
Institute of Aerodynamics and Flow Technology,
German Aerospace Center (DLR)
Bunsenstr. 10, D-37073 Göttingen, Germany
matthias.kaczorowski@dlr.de

**Claus Wagner**
Institute of Aerodynamics and Flow Technology,
German Aerospace Center (DLR)
Bunsenstr. 10, D-37073 Göttingen, Germany
claus.wagner@dlr.de

## ABSTRACT

In the present study Rayleigh-Bénard convection within a rectangular cell is analysed. Turbulent Rayleigh numbers up to $Ra = 6.0 \times 10^8$ have been simulated using Direct Numerical Simulations (DNS) and Large Eddy Simulations (LES) employing the tensor diffusivity model by Leonard and Winkelmans (1999). The effective exponent of the Nusselt-Rayleigh relation is found to be 0.284 which matches theroretical and experimental predections of $2/7$ ($\approx 0.286$) very well. Furthermore, the thermal dissipation rate distribution is investigated based on the approach by Shishkina and Wagner (2006). The distribution function is found to consist of three distinct regimes featuring the thermal turbulent background, the plumes and the conductive sublayer. Two functions are defined to approximate the distribution of the turbulent background and the conductive sublayer, and hence limits could be defined for the integration of the three regions. With these limits it is possible to quantify the respective contributions of the different parts of the flow field showing that the contributions of the turbulent background up to $Ra = 6.0 \times 10^8$ are very small but increse rapidly, once a fully developed turbulent field is established. For the highest simulated Rayleigh number it occupies more than 80% of the fluid volume.

## INTRODUCTION

A well-studied, but yet not fully understood problem in fluid mechanics is the Rayleigh-Bénard convection, where fluid between horizontal walls is heated from below and cooled from above.

In recent studies Verzicco and Camussi (1999, 2003) have carried out numerical simulations of turbulent convection within cylindrical containers of low aspect ratio $\Gamma = D/H$. They found that for a container of aspect ratio unity and $Pr = 0.7$ there is a transition from $\delta_\theta > \delta_u$ to $\delta_\theta < \delta_u$ around $Ra = 2 \times 10^7$, where $\delta_\theta$ and $\delta_u$ denote the thermal and the kinetic boundary layer thickness, respectively. This observation matches Grossmann and Lohse's theory (2000). However, they point out that according to theoretical analysis this transition should not occur until $Ra = O(10^8)$. They also suggested that the thermal dissipation rates should be divided into contributions from plumes and background turbulence.

Shishkina and Wagner (2006) have conducted direct simulations of Rayleigh-Bénard convection in a wide cylindrical geometry. They analysed the contribution of thermal dissipation rates due to the turbulent background and the plumes, confirming Grossman and Lohse's refined theory (2004) by showing that the influence of the thermal turbulent background on the flow field increases with increasing $Ra$.

However, the analysis of thermal dissipation rates was only carried out qualitatively. Therefore the aim of the present study is to investigate the distribution of the thermal dissipation rates and their respective contribution to the mean thermal dissipation rate. Furthermore, contributions from the turbulent background, plumes and boundary layers are evaluated for different Rayleigh numbers.

## COMPUTATIONAL SETUP

The incompressible Navier-Stokes equations are solved in dimensionless form

$$\begin{aligned} \frac{\partial u_i}{\partial x_i} &= 0 \\ \frac{\partial u_i}{\partial t} &= -u_i \frac{\partial u_i}{\partial x_i} - \frac{\partial p}{\partial x_i} + \sqrt{\frac{Pr}{\Gamma^3 Ra}} \frac{\partial^2 u_i}{\partial x_i^2} + \theta\, \delta_{1i} \quad (1) \\ \frac{\partial \theta}{\partial t} &= -u_i \frac{\partial \theta}{\partial x_i} + \sqrt{\frac{1}{\Gamma^3 RaPr}} \frac{\partial^2 \theta}{\partial x_i^2} \end{aligned}$$

where $u_i$ are the velocity components in $i$-direction, $\theta$ and $p$ represent the temperature and pressure, respectively, and $\delta_{ij}$ is the Kronecker symbol. In this particular case gravitational forces are acting in the $x_1$-direction, i.e. the vertical direction. The non-dimensional constants $Pr = \nu/\kappa$, $Ra = \alpha g H^3 \Delta T/(\nu\kappa)$ and $\Gamma = W/H$ are defined by the kinematic viscosity $\nu$, the thermal diffusivity $\kappa$, the thermal expansion coefficient $\alpha$, the temperature difference between top and bottom walls $\Delta T$ and the height $H$ and width $W$ of the fluid layer. Density variations are accounted for through the Boussinesq approximation.

Schumann's volume balance procedure is used for the integration over the fluid cells and the solution is evolved in time by means of the Euler-Leapfrog scheme. Spatial derivatives are approximated by fourth order accurate central differences where the velocity components are stored on staggered grids. For more detail on the spatial discretisation the reader is refered to Shishkina and Wagner (2007).

Table 1: Grid resolution in the centre of the cell.

| Ra | $Nu$ | $\eta_k$ | $h_{DNS}$ |
|---|---|---|---|
| $3.5 \times 10^5$ | 6.15 | $7.17 \times 10^{-2}$ | $3.01 \times 10^{-2}$ |
| $3.5 \times 10^6$ | 11.9 | $3.34 \times 10^{-2}$ | $1.72 \times 10^{-2}$ |
| $3.5 \times 10^7$ | 22.9 | $1.58 \times 10^{-2}$ | $1.06 \times 10^{-2}$ |
| $2.3 \times 10^8$ | 39.5 | $8.57 \times 10^{-3}$ | $9.99 \times 10^{-3}$ |
| $6.0 \times 10^8$ | 55.2 | $6.17 \times 10^{-3}$ | $9.99 \times 10^{-3}$ |

The horizontal walls are assumed to be isothermal with non-dimensional temperatures $\theta_l = +0.5$ and $\theta_u = -0.5$ at the hot and the cold wall, respectively. The adiabatic lateral walls are implemented by means of a zero temperature gradient perpendicular to the wall, i.e. $\partial\theta/\partial z = 0$. No-slip conditions are used for the solid walls, so that velocities in $i$-direction $u_i|_{\text{wall}} = 0$ and periodic boundary conditions are employed in longitudinal direction.

The flow field is initialised with a quiescent velocity field and the conduction profile for the temperature field. Additionally, small disturbances are superimposed onto the temperature field in order to excite instabilities, and hence to trigger convection.

In order to sufficiently resolve the boundary layers the grid points are clustered in the vicinity of the walls using a hyperbolic tangential, so that a minimum of eight grid pints are within the boundary layer and the grid spacing $h_{DNS} = (\Delta x_i \Delta x_j \Delta x_k)^{1/3}$ in the core region satisfies Grötzbach's (1983) estimate for the Kolmogorov scales $\eta_k$.

$$h_{DNS} \leq \eta_k = \frac{\pi}{\Gamma} \frac{\sqrt{Pr}}{((Nu-1)Ra)^{1/4}} \tag{2}$$

However, for the largest Rayleigh numbers well-resolved Large Eddy Simulations (LES) rather than Direct Numerical Simulations (DNS) have been performed. For the LES the tensor diffusivity model by Leonard and Winkelmans (1999) is used to account for the subgrid scales.

The solution is evolved in time until the flow field is in equilibrium, i.e. heat transfer between hot and cold walls and turbulence intensity have reached a statistically steady state. For the evaluation of the Nusselt mumber the data is averaged in time and space (periodic direction) during the subsequent processing. Energy spectra are extracted from the periodic direction and averaged in time.

## RESULTS

Figure 1 shows snapshots of isothermal surfaces for various Rayleigh numbers. It can be seen that the thermal boundary layers at the top and bottom walls become thinner and the structures of rising and falling fluid become smaller as the Rayleigh number increases. For $Ra = 3.5 \times 10^5$, just after the transition to turbulence, the isothermal surfaces show a regular plume formation. Beyond $Ra = 3.5 \times 10^7$ the irregular plume distribution reflects a fully turbulent flow. The plumes have become significantly smaller and more equally distributed over the top and bottom plates.

### Scaling Law

Figure 2 illustrates Nusselt number $Nu$ as a function of Rayleigh number from the onset of convection to $Ra = 6.0 \times 10^8$. At $Ra = 8.8 \times 10^4$ the flow field has become three dimensional and time-dependent. For higher Rayleigh numbers transition occurs and a turbulent flow is established.

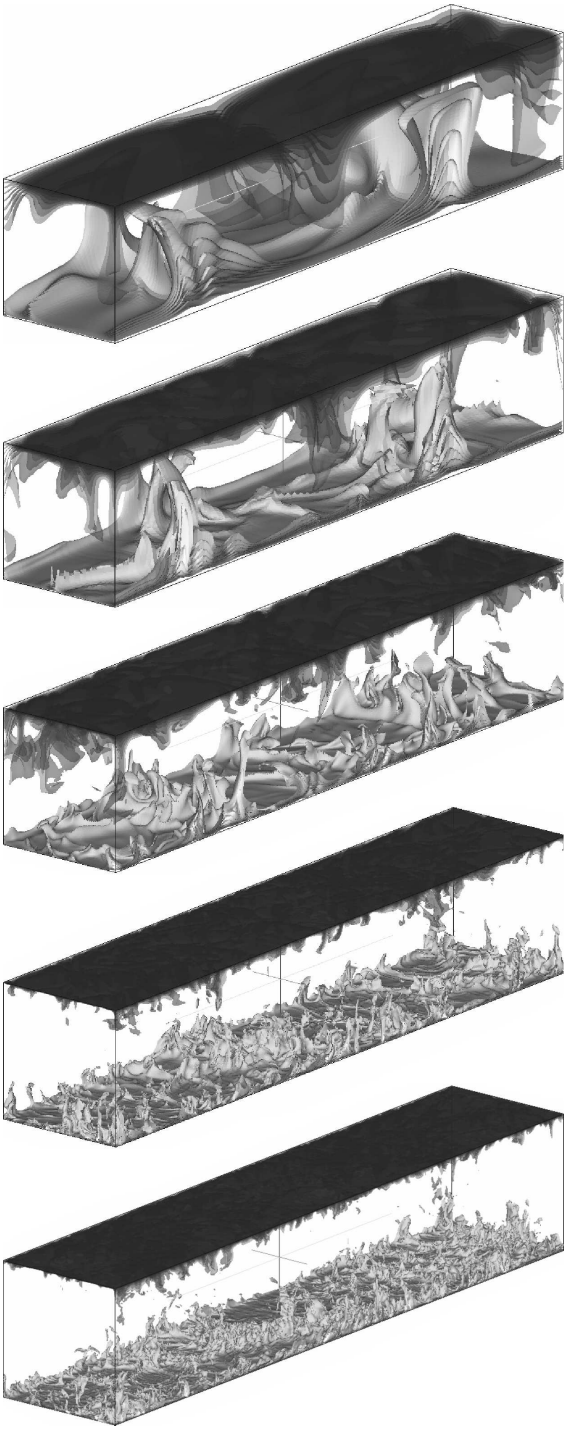

Figure 1: Isometric view of 12 isothermal surfaces in the convection cell with $H : L : W = 1 : 5 : 1$ for Rayleigh numbers; $Ra = 3.5 \times 10^5$, $Ra = 3.5 \times 10^6$, $Ra = 3.5 \times 10^7$, $Ra = 2.3 \times 10^8$ and $Ra = 6.0 \times 10^8$ (top to bottom). Hot fluid ($\theta = +0.5$) is white and cold fluid ($\theta = -0.5$) black.

It is evident that an effective scaling $Nu \sim Ra^{-0.284}$ is obtained for $3.5 \times 10^5 \leq Ra \leq 6.0 \times 10^8$ which matches Grossmann and Lohse's (2004) prediction of $Nu \sim Ra^{0.286}$ for fluids with $Pr \approx 1$ very well.

### Energy Spectra

Figure 3 shows thermal and kinetic energy spectra taken

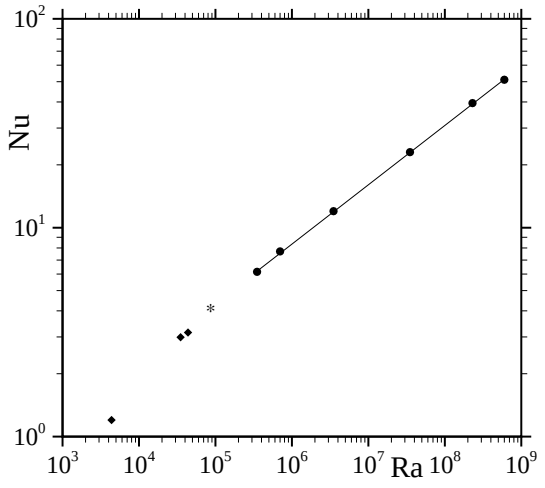


Figure 2: Nusselt number $Nu$ as a function of Rayleigh number $Ra$. laminar 2-D flow (♦), time-dependent 3-D flow (∗), turbulent flow (•) and $Nu \sim Ra^{0.284}$ (—).

from probes in the centre of the cell, averaged in time and in periodic direction. It is observed that the temperature spectra match the Bolgiano exponent (Bolgiano, 1959) of 7/5, but lack the inertial subrange which is supposed to follow the buoyancy subrange. According to the Bolgiano dynamics the velocity spectra would show a 11/5 decrease within the buoyancy subrange, however, only the Kolmogorov-law is observed. This is in agreement with results by Verzicco and Camussi (2003) who argued that this might be the case, when most of the thermal energy is injected into the large scales through the wind. On the other hand it has to be taken into account that the Bolgiano dynamics assume a stably stratified fluid layer which is not given in Rayleigh-Bénard convection where energy is injected into the fluid by means of thermal plumes which are the driving force for convection as shown by Xi et al. (2004). It is therefore reasonable that the velocity spectra follow the Kolmogorov law, since there is no energy extracted from the velocity field and stored as potential energy as suggested by Bolgianos theory.

Comparison of the two spectra illustrates that at $3.5\times10^5$ the flow has become turbulent, but the inertial subrange is yet very small and hard to distinguish, whereas a fully developed spectrum is obtained for $Ra = 3.5 \times 10^7$. However, it can be assumed that all relevant turbulent scales are resolved by the grid, since both the inertial subrange and the dissipation range can be identified from the kinetic energy spectra and the Batchelor scales of temperature are larger than the Kolmogorov scales; $\eta_B/\eta_k = Pr^{-3/4}$.

### Thermal Dissipation Rates

The thermal dissipation rates of the flow field have been analysed advancing the approach by to Shishkina and Wagner (2006), who defined two functions

$$\tau(\xi) = \langle \delta(\xi) \rangle_V \tag{3}$$

$$\sigma(\xi) = \frac{\langle \delta(\xi)\ \epsilon_\theta \rangle_V}{\langle \epsilon_\theta \rangle_V} \tag{4}$$

in order to evaluate the contribution of plumes and boundary layers to the volume averaged thermal dissipation rate $\langle \epsilon_\theta \rangle_V$. The function $\tau(\xi)$ defines the portion of the fluid occupied by thermal dissipation rates smaller than $\xi\ \epsilon_{\theta,\max}$ and $\sigma(\xi)$ is the contribution of this range of dissipation rates to the

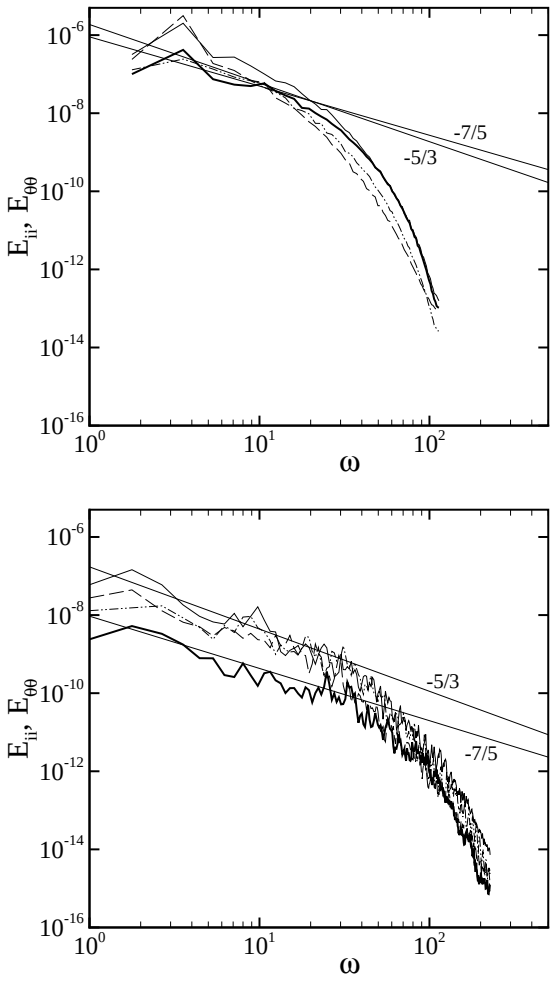


Figure 3: Energy spectra extracted from the centre of the convection cell for $Ra = 3.5 \times 10^5$ (top) and $Ra = 3.5 \times 10^7$ (bottom); $E_{uu}$ (—), $E_{vv}$ (- - -), $E_{ww}$ (-·-·-) and $E_{\theta\theta}$ (—).

volume averaged dissipation rate. The threshold function $\delta(\xi)$ is defined by

$$\delta(\xi) = \begin{cases} 1, & \text{if } \epsilon_\theta \le \xi\ \epsilon_{\theta,\max} \\ 0, & \text{otherwise} \end{cases} \tag{5}$$

Analysing Rayleigh-Bénard convection (RBC) in a cylindrical cell they found that the contribution of the thermal dissipation rates increases with $Ra$ for a fixed threshold $\xi$ and concluded that the thermal background dominates the flow field for $Ra \to \infty$.

In order to gain more detailed information on the distribution of the thermal dissipation rates and their contribution to the volume averaged mean in turbulent RBC, the dissipation rates are averaged over a small range of scales $\xi \pm \Delta$, so that the following threshold function is used.

$$\delta_\Delta(\xi) = \begin{cases} 1, & \text{if } (\xi - \frac{\Delta}{2}) \le \frac{\epsilon_\theta}{\epsilon_{\theta,\max}} < (\xi + \frac{\Delta}{2}) \\ 0, & \text{otherwise} \end{cases} \tag{6}$$

and the functions

$$\langle \epsilon_\theta \rangle_\xi = \frac{\langle \delta_\Delta(\xi)\ \epsilon_\theta \rangle_V}{\langle \epsilon_\theta \rangle_V} \tag{7}$$

$$V(\langle \epsilon_\theta \rangle_\xi) = \langle \delta_\Delta(\xi) \rangle_V \tag{8}$$

represent the contribution of the thermal dissipation rates to the volume averaged thermal dissipation rate $\langle \epsilon_\theta \rangle_V$ and their respective portion of the fluid volume.

Figure 4 (top) illustrates the distribution of $\langle \epsilon_\theta \rangle_\xi$ and $V(\langle \epsilon_\theta \rangle_\xi)$ as a function of $\xi$ for different Rayleigh numbers. It can be observed that the distributions of thermal dissipation rates have a distinct maximum whose position and height depends on the Rayleigh number of the flow. As $Ra$ increases its maximum is shifted towards smaller $\xi$ indicating that smaller dissipation rates contribute increasingly more to the volume averaged thermal dissipation rate than larger ones. On the other hand it can be seen from 4 (bottom) that small scales begin to inhabit an increasingly larger fraction of the fluid volume.

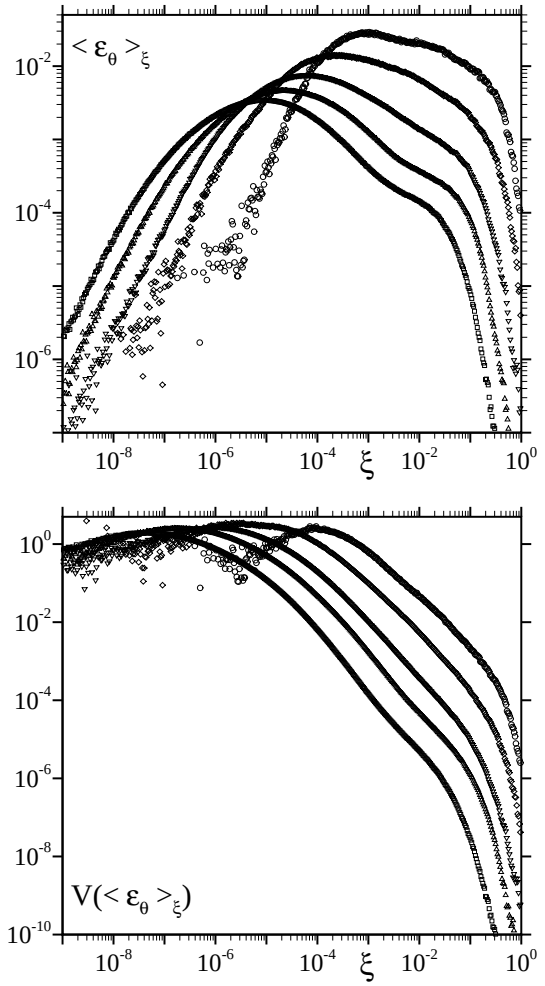


Figure 4: Distribution functions of the thermal dissipation rates (top) and their respective portion of the fluid (bottom) for $Ra = 3.5 \times 10^5$ ($\circ$), $Ra = 3.5 \times 10^6$ ($\diamond$), $Ra = 3.5 \times 10^7$ ($\triangledown$), $Ra = 2.3 \times 10^8$ ($\triangle$) and $Ra = 6.0 \times 10^8$ ($\square$).

In thermal convection the largest gradients are typically found within the boundary layers, therefore the highest thermal dissipation rates are also likely to be found in this region. Hence, it follows that contributions for $\xi \to 1$ are produced within the thermal boundary layers. On the other hand dissipation rates with $\xi \to 0$ are typically associated with the turbulent thermal background. Inspecting the distribution of $\langle \epsilon_\theta \rangle_\xi$ over $\xi$ reveals that there are three distinct regions, which are illustrated in Figure 5, where region *I* is considered to be the turbulent background, region *II* is dominated by the thermal plumes and region *III* by the conductive sublayer.

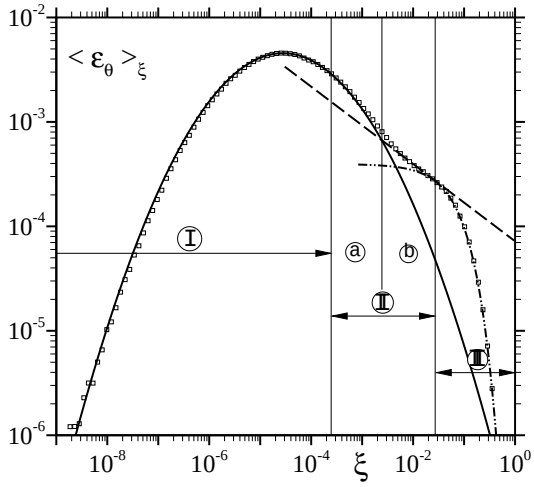


Figure 5: Schematic of a thermal dissipation rate distribution derived from $Ra = 2.3 \times 10^8$ data ($\square$) and its three regimes. Regime *I* which is associated with the thermal background follows a Gaussian-like distribution (—) and the near wall region, regime *III*, an exponential function (- ·· -). The intermediate regime *II* is associated with the themal plumes and outer boundary layer and subdivided into a power-law (– –) and a buffer region.

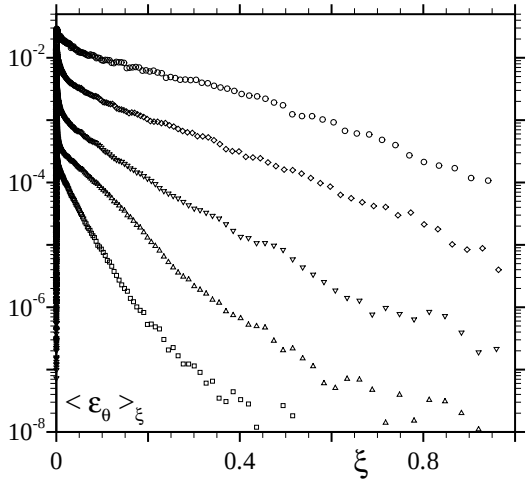


Figure 6: Distribution functions of the thermal dissipation rates in regime *I* for $Ra = 3.5 \times 10^5$ ($\circ$), $Ra = 3.5 \times 10^6$ ($\diamond$), $Ra = 3.5 \times 10^7$ ($\triangledown$), $Ra = 2.3 \times 10^8$ ($\triangle$) and $Ra = 2.3 \times 10^8$ ($\square$).

A more detailed analysis of the distribution function of $\langle \epsilon_\theta \rangle_\xi$ reveals that within region *III*

$$\langle \epsilon_\theta \rangle_\xi = a\, e^{-c\,\xi} \tag{9}$$

Furthermore, it is observed that $c \sim \log(RaPr)$ and $a \sim 1/\sqrt{RaPr}$, i.e. is the non-dimensional thermal conductivity. It is therfore concluded that regime *III* represents the conductive sublayer. Re-scaled plots of the dissipation rates in this region are presented in Figure 6. Since the data is extracted from instantaneous flow fields and the cell is of finite extend in periodic direction, the lines are not perfectly smooth, especially for $\xi \to 1$.

Table 2: Limits of $\xi$ for the integration of the three regions.

| Ra | *I-II* | *II-III* |
|---|---|---|
| $3.5 \times 10^5$ | $1.55 \times 10^{-3}$ | $4.40 \times 10^{-2}$ |
| $3.5 \times 10^6$ | $4.40 \times 10^{-4}$ | $6.90 \times 10^{-2}$ |
| $3.5 \times 10^7$ | $1.46 \times 10^{-4}$ | $4.27 \times 10^{-2}$ |
| $2.3 \times 10^8$ | $1.95 \times 10^{-4}$ | $2.63 \times 10^{-2}$ |
| $8.6 \times 10^8$ | $1.00 \times 10^{-4}$ | $1.16 \times 10^{-2}$ |

The turbulent thermal background which is found to be represented by regime *I* follows a Gaussian distribution with respect to $\log(\xi)$

$$\langle \epsilon_\theta \rangle_\xi \sim e^{-(\log(\xi/\xi_{\max}))^2} \tag{10}$$

Since regimes *I* and *III* are the thermal background and the conductive sublayer, respectively, regime *II* has to be the outer boundary layer (plumes are considered to be detached boundary layers). It is observed that this intermediate region does not have a similarly unique behaviour like regions *I* or *III*. However, it is found that for all Rayleigh numbers its upper limit can be fitted using a power-law. Figure 5 suggests that region *II* can be subdivided into two parts, of which *IIb* appears to define the roots, stems and plume tops, whereas *IIa* is considered the plume influenced region or the 'dead water' of the plumes.

Figure 7 confirms the assumption that regime *III* represents the conductive sublayer, since it can only be found in the near-wall region where there are almost equidistant isothermal lines. At locations where hot or cold fluid begins to rise or fall this layer bursts and a bubble of slightly lower dissipation rates (regime *IIb*) begins to drift away, immersed into regime *IIa* dissipation rates. Figure 7 illustrates that *II* correlates with the plumes of hot (or cold) rising (or falling) fluid. Further investigation reveals that *IIb* appears to define the roots, stems and plume tops, whereas *IIa* is considered the plume influenced region or the 'dead water' of the plumes.

In the following an attempt is made to quantify the respective contributions of the thermal turbulent background, plumes and boundary layers, i.e the above mentioned regimes *I*, *II* and *III*. This analysis is conducted for various Rayleigh numbers by integration of these regions. The boundary *I-II* is defined at the point where the data does not match the Gaussian fit anymore, whereas the limit *II-III* is set to be the intersection of the power-law and the exponential fit. The limits used for the integration are given by Table 2.

Comparing the limits of the integration as presented in Table 2 suggests that the plume dominated range of dissipation rates is decreasing when Rayleigh numbers beyond $3.5 \times 10^7$ are reached, whereas it is increasing for lower Rayleigh numbers. This is in agreement with the visual inspection of Figure 1, where it was observed that for $Ra < 3.5 \times 10^7$ a fully developed turbulent flow is obtained.

In Tables 3 and 4 the respective contributions of the thermal dissipation and their fraction of the fluid volume of regimes *I*, *II* and *III* are presented. The data indicates that the contribution of the turbulent background to the mean thermal dissipation rate is very small and significant changes can only be observed when $Ra = 2.3 \times 10^8$ is reached. The fraction of the fluid volume, on the other hand is constantly increasing with $Ra$ and at the highest Rayleigh number almost the entire fluid consists of background turbulence.

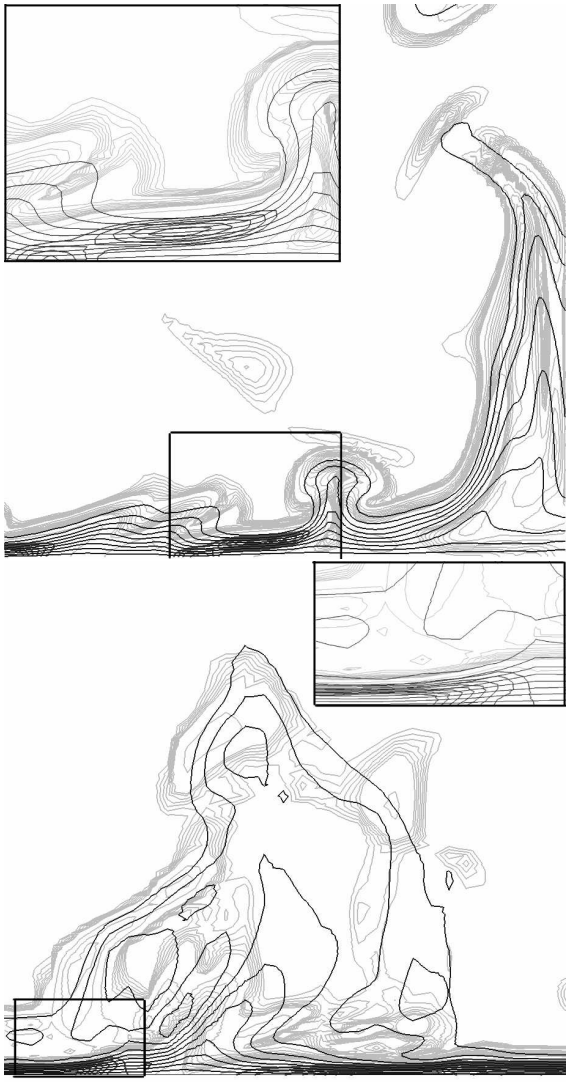

Figure 7: Close-up view of the thermal dissipation rate distribution in a vertical section through the cell. Isolines in dark grey represent regime *III* and light grey *II*. Isothermal lines (black) with $0.05 \leq |\theta| \leq 0.45$ are given for refenence; $Ra = 3.5 \times 10^7$ (top) and $Ra = 2.3 \times 10^8$ (bottom). The insets show close-up view of the conductive sublayer.

However, it has to be pointed out that due to the relatively small grid size, and hence insufficient data for the statistical analysis, the signal of $Ra = 3.5 \times 10^5$ is rather noisy as can be seen from Figure 4. Therefore these results need to be interpreted with caution.

The plumes seem to have a maximum in terms of their contribution as well as their volume for $Ra \approx 10^7$, which is reasonable since for $Ra \to 0$ and $Ra \to \infty$ there are no plumes. The conductive sublayer, on the other hand, has a minimum contribution around $Ra \approx 10^7$. Considering the volume inhabited by the the plumes it is observed that it maximises around $Ra = 3.5 \times 10^7$, which is plausible since there are no plumes below the onset of convection and for $Ra \to \infty$ the plumes are supposed to vanish again. The volume associated with the conductive sublayer is steadily decreasing and, neglecting the data point for $Ra = 3.5 \times 10^5$, following the scaling $\epsilon_{\theta,III} \sim \delta \sim Ra^{-0.284}$ confirming that this region is part of the boundary layer.

Table 3: Contribution of the thermal dissipation rates associated with the turbulent background ($I$), the plumes ($II$) and the conductive sublayers ($III$) to the volume averaged thermal dissipation rate obtained by partial integration of the distribution function of $\langle\epsilon_\theta\rangle_\xi$.

| Ra | $\epsilon_{\theta,I}$ | $\epsilon_{\theta,II}$ | $\epsilon_{\theta,III}$ |
|---|---|---|---|
| $3.5 \times 10^5$ | 0.011 | 0.215 | 0.774 |
| $3.5 \times 10^6$ | 0.008 | 0.444 | 0.548 |
| $3.5 \times 10^7$ | 0.009 | 0.467 | 0.525 |
| $2.3 \times 10^8$ | 0.027 | 0.411 | 0.562 |
| $8.6 \times 10^8$ | 0.037 | 0.388 | 0.575 |

Table 4: Portion of the fluid containing thermal dissipation rates $\epsilon_\theta(\xi)$ associated with the turbulent background ($I$), the plumes ($II$) and the conductive sublayers ($III$) obtained by partial integration of the distribution function of $V(\langle\epsilon_\theta\rangle_\xi)$.

| Ra | $V(\epsilon_{\theta,I})$ | $V(\epsilon_{\theta,II})$ | $V(\epsilon_{\theta,III})$ |
|---|---|---|---|
| $3.5 \times 10^5$ | 0.448 | 0.434 | 0.118 |
| $3.5 \times 10^6$ | 0.504 | 0.482 | 0.028 |
| $3.5 \times 10^7$ | 0.589 | 0.397 | 0.014 |
| $2.3 \times 10^8$ | 0.795 | 0.195 | 0.010 |
| $8.6 \times 10^8$ | 0.850 | 0.143 | 0.007 |

## CONCLUDING REMARKS

Turbulent Rayleigh-Bénard convection within a periodic rectangular cell has been investigated by means of DNS and LES. It was shown that the *Nu-Ra* relation is in good agreement with Grossmann and Lohse's (2004) prediction. Kinetic energy spectra extracted from the centre of the cell match the 5/3-law within the inertial subrange and a steep gradient is obtined towards the cut-off wave number, indicating that (in the case of DNS) the spatial resolution of the computational mesh is fine enough to resolve all relevant turbulent scales.

The distribution of the thermal dissipation rates and their respective fraction of the fluid volume was analysed. It was found that the maximum of the distribution function is shifted towards smaller scales as Rayleigh number increased and that the dissipation rates are more equally distributed once the flow has become fully turbulent. Furthermore, the distribution function was subdivided into three regimes that represent the turbulent thermal backgound, the thermal plumes and the conductive sublayer. Partial integration of the distribution functions were performed in order to quantify the contributions of the respective regions. It was found that at low Rayleigh numbers the thermal background contributes only very little to the volume averaged thermal dissipation rate, but at the highest simulated Rayleigh numbers a significant increase was observed when the impact of the plumes begins to decrease again. Once a fully developed turbulent flow is established the portion of the fluid inhabited by the turbulent background rapidly increases to 80% and more 'consuming' the volume of the plume which are strongest and largest when the fully developed turbulent flow is established.

The present study confirms the assumption that the contribution of the turbulent thermal background to the volume averaged mean increases. However, for Rayleigh numbers up to $6.0 \times 10^8$ its contribution is still very small compared to those of plumes and boundary layers.

## REFERENCES


Bolgiano, R., 1959, "Turbulent Spectra in a stably stratified Atmosphere", *J. Geophys. Res.*, Vol. 64(12), pp. 2226-2229.

Grossmann, S. and Lohse, D., 2000, "Scaling in thermal convection: a unifying theory", *J. Fluid Mech.*, Vol. 407, pp. 27-56.

Grossmann, S. and Lohse, D., 2004, "Fluctuations in turbulent Rayleigh-Bénard convection: The role of plumes", *Phys. Fluids*, Vol. 16(12), pp. 4462-4472.

Grötzbach, G., 1983, "Spatial Resolution Requirements for Direct Numerical Simulation of Rayleigh-Bénard Convection", *J. Comp. Phys.*, Vol. 49, pp. 241-264.

Leonard, A. amd Winkelmans, G. S., 1999, "A tensor-diffusivity subgrid model for Large-Eddy Simulation", Tech. Rep. 043, cit-asci-tr043, Caltech ASCI.

Shishkina, O., and Wagenr, C., 2007, "A fourth order finite volume scheme for turbulent flow simulations in cylindrical domains", *Computers and Fluids*, Vol. 36(2), pp. 484-497.

Shishkina, O., and Wagner, C., 2006, "Analysis of thermal dissipation in turbulent Rayleigh-Bénard convection", *J. Fluid Mech.*, Vol. 546, pp. 51-60.

Verzicco, R., and Camussi, R., 1999, "Prandtl number effects in convective turbulence", *J. Fluid Mech.*, Vol. 383, pp. 55-73.

Verzicco, R., and Camussi, R., 2003, "Numerical experiments on strongly turbulent thermal convection in a slender cylindrical cell", *J. Fluid Mech.*, Vol. 477, pp. 19-49.

Xi, H.-D., Lam, S., Xia, K.-Q., 2004, "From laminar plumes to organised flows: the onset of large-scale circulation in turblent thermal convection", *J. Fluid Mech.*, Vol. 503, pp. 47-56.